

Continuous Bayesian probability estimator in predictions of nuclear charge radii*

Kaizhong Tan,¹ Lei Wang,² Wanqing Gao,¹ Tianshuai Shang,³ Jian Li,³ Chang Xu,⁴ and Jian Liu^{1,†}

¹College of Science, China University of Petroleum (East China), Qingdao 266580, China

²School of Physics Science and Engineering, Tongji University, Shanghai 200092, China

³College of Physics, Jilin University, Changchun 130012, China

⁴Department of Physics, Nanjing University, Nanjing 210093, China

Recently, machine learning has become a powerful tool for predicting nuclear charge radius R_C , providing novel insights into complex physical phenomena. This study employs the continuous Bayesian probability (CBP) estimator and the Bayesian model averaging (BMA) to optimize the predictions of R_C from sophisticated theoretical models. The CBP estimator treats the residual between the theoretical and experimental values of R_C as a continuous variable, deriving its posterior probability density function (PDF) from Bayesian theory. The BMA method assigns weights to models based on their predictive performance for benchmark nuclei, thereby accounting for each model's unique strengths. In global optimization, the CBP estimator improves the predictive accuracy of the three theoretical models by about 60%. In extrapolation analyses, it consistently achieves an improvement rate of approximately 45%, demonstrating the robustness of the CBP estimator. Furthermore, the combination of the CBP and BMA methods reduces the standard deviation to below 0.02 fm, effectively reproducing the pronounced shell effects on R_C of the Ca and Sr isotope chains. The studies in this paper propose an efficient way to accurately describe R_C of unknown nuclei, with potential applications to research on other nuclear properties.

Keywords: Machine learning, Nuclear charge radii, Continuous Bayesian probability estimator, Bayesian model averaging.

I. INTRODUCTION

The nuclear charge radius R_C is a fundamental property of atomic nuclei, playing a crucial role in researching nuclear structure [1]. It provides insights into various phenomena, including shape coexistence [2], neutron skin [3, 4], proton halo [5], shell structure [6], odd-even staggering [7, 8] and nuclear matter saturation [9], etc. There are mainly two types of experimental methods for measuring R_C . One type directly determines R_C through experiments such as muonic atom X-ray spectroscopy (μ^-) [10] and high-energy elastic electron scattering (e^-) [11, 12]. Another type analyzes subtle differences between isotopes to indirectly measure R_C , for instance, K_α X-ray isotope shifts (K_α IS) [13] and optical isotope shift (OIS) [14]. Recently, advancements in laser spectroscopy techniques have enabled the precise determination of R_C for over 130 unstable nuclei [15–20]. Nevertheless, challenges in the experimental measurement of R_C persist, especially in the production of exotic isotopes and improving experimental sensitivity, making it difficult to understand nuclear structures in unexplored regions.

Many theoretical models have been developed to study R_C , from macroscopic formulas to sophisticated microscopic approaches. First of all, a conventional approach to estimate R_C is the semi-empirical formula based on the $A^{1/3}$ law of the liquid drop model, improved by introducing effects such as shell structure, isospin, and odd-even nuclear effects

[21, 22]. Subsequently, local-relation-based models determine R_C from the properties of neighboring nuclei [23–26], with prominent examples being the Garvey-Kelson relation [27, 28] and the mirror nuclei relation [29, 30]. In addition, more sophisticated mean-field nuclear structure models offer self-consistent descriptions of R_C and other nuclear properties. Examples include the Skyrme-Hartree-Fock-Bogoliubov (HFB) models [31–33], the relativistic mean-field (RMF) models [34–36], and the relativistic Hartree-Bogoliubov (RHB) models [37–39]. Lastly, a class of *ab initio* approaches, such as the no-core shell model (NCSM), starts from realistic nucleon interactions, providing a precise description of R_C by solving the many-body Schrödinger equation or the corresponding self-consistent field equations [40, 41]. Theoretical models have achieved significant advancements, reducing root-mean-square errors to below 0.05 fm and providing satisfactory descriptions of the unique behaviors of R_C in isotope chains. However, as the accuracy requirements for calculations increase, the complexity of theoretical models also grows significantly.

In recent years, machine learning (ML) techniques have gained widespread application in nuclear physics [42, 43], including studies on nuclear masses [44–51], charge density distributions [52, 53], nuclear decay [54–57], and nuclear reaction [58–60], particularly in predicting R_C [61–68]. Initially, the ML method was applied to directly train on experimental values of R_C , independent of theoretical models. As early as 2013, researchers utilized artificial neural networks (ANN) to predict R_C by directly generating a formula [61]. Subsequently, to incorporate the strengths of theoretical models, ML techniques were employed to refine them by estimating the residuals between theoretical and experimental values of R_C . Early work in 2016 proposed a Bayesian neural network (BNN) with a single hidden layer to optimize these predictions [62]. Later, multiple research groups significantly enhanced the robustness of BNN by introducing

* This work was supported by the National Natural Science Foundation of China (Grants No. 12475135, No. 12035011 and No. 12475119), by the Shandong Provincial Natural Science Foundation, China (Grant No. ZR2020MA096), and by the Fundamental Research Funds for the Central Universities (Grant No. 22CX03017A).

† Corresponding author: liujian@upc.edu.cn

physical effects and adding input features [63–66]. Notably, the naive Bayesian probability (NBP) classifier, which applies Bayesian theory and *k-means* clustering, reframes the prediction of R_C as a classification task. This approach demonstrates strong extrapolation capabilities and provides uncertainty in prediction [68, 69].

Recently, the application of the continuous Bayesian probability (CBP) estimator and the Bayesian model averaging (BMA) has further improved the reliability of nuclear mass descriptions [70]. Unlike the NBP method, which discretizes the residuals δ of the theoretical model, the CBP estimator treats δ as a continuous variables. By combining the Bayesian framework with kernel density estimation (KDE), the CBP estimator derives the posterior probability density function (PDF) of δ for target nuclei. This method demonstrates robust predictive performance and can explain intrinsic numerical relationships. Moreover, the BMA method combines the predictive strengths of different theoretical models across distinct regions of the nuclear chart, further improving overall performance [71–73].

This study combines the CBP estimator and the BMA method to optimize the predictions of R_C . The initial theoretical values of R_C are separately calculated by the HFB model, the RHB model, and the semi-empirical liquid drop model. First, the global optimization capability of the CBP estimator is evaluated by comparing its predictions with experimental data from the 2013 compilation of nuclear charge radii [15]. Subsequently, its extrapolation capability is investigated using the learning set from the 2004 compilation [10] to predict R_C for nuclei newly reported in the 2013 compilation. After optimization by the CBP estimator, to further improve predictive accuracy for nuclei near the drip line, the BMA method is applied to assign weights to each model based on their predictive performance on the benchmark nuclei. The benchmark nuclei selected in this study are ^{49}K [74], ^{38}Ca [75], ^{119}Cd [76], and ^{201}Po [77]. Finally, we predict R_C of the Ca and Sr isotopic chains using the CBP estimator in combination with the BMA method, to verify the ability of this approach to capture the physical effects on R_C . The approaches proposed in this paper can be used to investigate R_C of unknown nuclei, with potential applications in the study of other nuclear properties.

This paper is structured into three sections: Sect. II introduces the theoretical framework of the CBP and BMA methods. Sect. III presents the results of these methods. Sect. IV provides the summary of this study.

II. THEORETICAL FRAMEWORK

The theoretical framework offers detailed procedures and formulas for the continuous Bayesian probability (CBP) estimator and the Bayesian model averaging (BMA). The method for evaluating predictive performance and the formula for quantifying uncertainties are also presented.

A. The continuous Bayesian probability method

In the CBP estimators, the residuals δ of R_C are treated as continuous variables, and their posterior PDFs are derived from Bayesian theory. Then, the estimated residuals, which are used to correct theoretical models, can be calculated from the posterior PDFs.

For continuous multivariate variables, given a set of features or variables X_1, X_2, \dots, X_m and a target variable Y , the posterior PDF can be expressed as

$$p(Y|X) = \frac{p(X_1|Y)p(X_2|Y) \cdots p(X_m|Y)p(Y)}{\int p(X_1|Y)p(X_2|Y) \cdots p(X_m|Y)p(Y)dY}. \quad (1)$$

The conditional PDF $p(X_i|Y)$ represents the likelihood of observing events X_i given the occurrence of Y , while the prior PDF $p(Y)$ denotes the frequency of occurrence for a given Y . The denominator in Eq. (1) acts as a normalization constant, ensuring that the posterior PDF $p(Y|X)$ integrates to unity.

According to Eq. (1), the event Y represents the continuous residual δ . The events X_i correspond to the proton number Z_t and the neutron number N_t of the target nucleus. Assuming that Z_t and N_t are independent of other variables. Thus, the posterior PDF can be expressed as follows:

$$p(\delta|Z_t, N_t) = \frac{p(Z_t|\delta)p(N_t|\delta)p(\delta)}{\int p(Z_t|\delta)p(N_t|\delta)p(\delta)d\delta}. \quad (2)$$

The conditional PDFs $p(Z_t|\delta)$ and $p(N_t|\delta)$ in Eq. (2) can be derived using the univariate Bayesian formula,

$$p(Z_t|\delta) = \frac{p(\delta|Z_t)p(Z_t)}{p(\delta)}, \quad (3)$$

$$p(N_t|\delta) = \frac{p(\delta|N_t)p(N_t)}{p(\delta)}. \quad (4)$$

In Eqs. (3) and (4), the prior probability $p(Z_t(N_t))$ is calculated from the occurrence frequencies of $Z_t(N_t)$ in the learning set. The likelihood PDFs $p(\delta|Z_t)$ and $p(\delta|N_t)$ are estimated through kernel density estimation (KDE).

$$p(\delta|Z_t) = \frac{1}{n_Z h_Z} \sum_{i=1}^{n_Z} K\left(\frac{\delta - \delta_i}{h_Z}\right), \quad (5)$$

$$p(\delta|N_t) = \frac{1}{n_N h_N} \sum_{i=1}^{n_N} K\left(\frac{\delta - \delta_i}{h_N}\right), \quad (6)$$

where $h_{Z(N)}$ denotes the bandwidth parameter, and $n_{Z(N)}$ represents the number of nuclei in the learning set that have the same $Z_t(N_t)$ as the target nucleus. The kernel function $K(t)$ is specified as a Gaussian kernel since the residuals follow a Gaussian distribution,

$$K(t) = \frac{1}{\sqrt{2\pi}} e^{-\frac{t^2}{2}}. \quad (7)$$

Similarly, the prior PDF $p(\delta)$ can also be obtained by KDE,

$$p(\delta) = \frac{1}{nh_\delta} \sum_{i=1}^n K\left(\frac{\delta - \delta_i}{h_\delta}\right), \quad (8)$$

where h_δ denotes the bandwidth parameter, and n is the total number of nuclei in the learning set. In Eqs. (5), (6), and (8), the individual residual δ_i is defined as $\delta_i = R_{C,i}^{\text{exp}} - R_{C,i}^{\text{th}}$. The values chosen for the bandwidth parameters h_δ , h_Z , and h_N depend on several factors, including the range of δ_i , the size of the dataset, and the level of noise in the data.

When determining the likelihood PDF and the prior PDF, a weight function is introduced to account for the local relationship between the neighboring nuclei:

$$w(Z, N; Z_t, N_t) = \exp\left[-\frac{(Z - Z_t)^2 + (N - N_t)^2}{\rho}\right] + \varepsilon. \quad (9)$$

The parameter ρ significantly impacts the prediction performance and extrapolation range of the CBP estimator. Based on the distribution characteristics of nuclei from the dataset on the nuclear chart, $\rho = 4$ is selected for this study. The parameter ε affects the stability of the posterior PDF, and $\varepsilon = 10^{-10}$ is chosen to ensure a Gaussian distribution for $p(\delta|Z_t, N_t)$. Then the prior PDF and likelihood PDF with the applied weights are as follows:

$$p_{\text{wt}}(\delta) = \frac{1}{nh_\delta} \sum_{i=1}^n K\left(\frac{\delta - \delta_i}{h_\delta}\right) w(Z_i, N_i; Z_t, N_t), \quad (10)$$

$$p_{\text{wt}}(\delta|Z_t) = \frac{1}{n_Z h_Z} \sum_{i=1}^{n_Z} K\left(\frac{\delta - \delta_i}{h_Z}\right) w(Z_i, N_i; Z_t, N_t), \quad (11)$$

$$p_{\text{wt}}(\delta|N_t) = \frac{1}{n_N h_N} \sum_{i=1}^{n_N} K\left(\frac{\delta - \delta_i}{h_N}\right) w(Z_i, N_i; Z_t, N_t). \quad (12)$$

The posterior PDF $p(\delta|Z_t, N_t)$ is obtained by combining Eqs. (2)-(12), and the expectation value is used to determine the estimated residual of the target nucleus

$$\delta^{\text{em}}(Z, N) = \int \delta p(\delta|Z, N) d\delta. \quad (13)$$

Ultimately, the refined nuclear charge radius value is obtained by appending the estimated residual $\delta^{\text{em}}(Z, N)$ to the theoretical nuclear charge radius $R^{\text{th}}(Z, N)$:

$$R_C^{\text{corr}}(Z, N) = R_C^{\text{th}}(Z, N) + \delta^{\text{em}}(Z, N). \quad (14)$$

B. Bayesian model averaging

Even after refinement by the CBP estimator, individual models often fail to comprehensively account for all physical

phenomena due to their varying strengths and weaknesses in different regions of the nuclear chart. To combine the optimal predictive performance of each model, the Bayesian model averaging (BMA) is introduced.

The BMA method is based on the Bayesian theorem, assigning weights to each model by assessing its predictive performance. Specifically, given a set of K candidate models M_1, \dots, M_K , the BMA method calculates posterior probabilities based on the predictions for the benchmark nucleus from each model. These posterior probabilities serve as the weights for each model, calculated as follows:

$$P(M_k|D) = \frac{P(D|M_k)P(M_k)}{\sum_{i=1}^K P(D|M_i)P(M_i)}. \quad (15)$$

In this paper, the four selected benchmark nuclei in dataset D are ^{49}K , ^{38}Ca , ^{119}Cd , and ^{201}Po , which are utilized to evaluate the accuracy of models based on the entire nuclide chart. Residuals are obtained using three theoretical models: the HFB model with SLy4 parameterization, the RHB model with the PK1 parameter set, and the semi-empirical liquid drop model. The prior probability $P(M_k) = 1/K$ is related to the number of candidate models, and the conditional probability $P(D|M_k)$ depends on the predictive performance of each theoretical model,

$$P(D|M_k) = \prod_j \frac{1}{\sqrt{2\pi}\mu} \exp\left[-\frac{(\delta_{k,j}^{\text{corr}})^2}{2\mu^2}\right], \quad (16)$$

where J represents the total number of benchmark nuclei. The refined residuals $\delta_{k,j}^{\text{corr}}$ for the j -th benchmark nucleus corresponding to the theoretical model M_k are defined as $\delta_{k,j}^{\text{corr}} = R_{k,j}^{\text{exp}} - R_{k,j}^{\text{corr}}$. The parameter μ is used to normalize the values of $\delta_{k,j}^{\text{corr}}$ and is defined by

$$\mu = \sqrt{\frac{1}{K \cdot J} \sum_{k=1}^K \sum_{j=1}^J (\delta_{k,j}^{\text{corr}})^2}. \quad (17)$$

Finally, the average nuclear charge radius calculated using the BMA method is:

$$\bar{R}(Z_t, N_t) = \sum_{i=1}^K R_{C,i}^{\text{corr}} P(M_i|D). \quad (18)$$

The discrepancies between the corrected theoretical predictions and the experimental data for each model are assessed using the standard deviation σ_{rms} , defined as

$$\sigma_{\text{rms}}^2 = \frac{1}{n} \sum_{i=1}^n (R_{C,i}^{\text{exp}} - R_{C,i}^{\text{corr}})^2. \quad (19)$$

In the CBP estimator, prediction uncertainties are obtained from the posterior PDF. The one-sigma uncertainty $\sigma^{\text{em}}(Z, N)$ of each model corresponding to the specific nucleus (Z, N) is defined as

$$\sigma^{\text{em}}(Z, N) = \sqrt{\int [\delta - \delta^{\text{em}}(Z, N)]^2 p(\delta|Z, N) d\delta}, \quad (20)$$

and the uncertainty of BMA is given by

$$\sigma^{\text{BMA}}(Z, N) = \sum_{i=1}^K \sigma_i^{\text{em}} P(M_i | D). \quad (21)$$

III. RESULTS

In this section, theoretical values of R_C are initially calculated using the HFB model with SLy4 parameterization, the RHB model with the PC-PK1 parameter set [78], and the three-parameter semi-empirical formula of Sheng *et al.* [22]. Notably, the RHB model is based on relativistic continuum Hartree-Bogoliubov theory and incorporates nucleon intrinsic electromagnetic structure corrections [79, 80]. Subsequently, the initial results are refined employing the CBP estimator and the BMA method. The entire set comprises 892 nuclei with proton numbers $Z > 3$, sourced from the 2013 charge radii compilation [15]. The global optimization and extrapolation capabilities of the CBP estimator are evaluated, followed by an analysis of the extrapolation performance of the approach that combines the CBP and BMA methods.

A. Global optimizations of the CBP estimator

Theoretical R_C values of 892 nuclei are calculated using three models, with the raw residuals $\delta^{\text{pre}} = R_C^{\text{exp}} - R_C^{\text{th}}$ for each nucleus are obtained. Subsequently, the CBP estimator is applied to refine the predictions of each model. According to Sect. II, the posterior PDF $p(\delta | Z_t, N_t)$ of the target nucleus can be calculated by Eqs. (2)-(12). The refined charge radius $R_C^{\text{corr}}(Z_t, N_t)$ is then obtained through Eqs. (13) and (14). In the entire set, the majority of δ^{pre} are distributed within the range of -0.1 fm to 0.1 fm. For nuclei with identical proton or neutron numbers, the variation in δ^{pre} is typically limited to within 0.05 fm. Based on the distribution characteristics of δ^{pre} , the bandwidth parameters were ultimately selected to be $h_\delta = 0.07 \text{ fm}^{-1}$, $h_Z = 0.01 \text{ fm}^{-1}$, and $h_N = 0.02 \text{ fm}^{-1}$. Table 1 presents the standard deviations σ_{pre} of the three theoretical models before optimization, and σ_{post} after optimization by the CBP estimator. The global optimization performance of the CBP estimator is evaluated using the improvement rate $\Delta\sigma/\sigma_{\text{pre}} = (\sigma_{\text{pre}} - \sigma_{\text{post}})/\sigma_{\text{pre}}$.

Table 1. The standard deviation σ_{pre} (fm) from the theoretical models and σ_{post} (fm) after the CBP and NBP refinements. 892 nuclei in 2013 charge radii compilation with $Z > 3$ are chosen as the entire set.

Methods	Models	HFB	RHB	Sheng
CBP	σ_{pre}	0.040	0.047	0.042
	σ_{post}	0.016	0.017	0.016
	$\Delta\sigma/\sigma_{\text{pre}}$	60.0%	63.8%	61.9%
NBP	σ_{post}	0.020	0.021	0.023
	$\Delta\sigma/\sigma_{\text{pre}}$	50.0%	55.3%	45.2%

As shown in Table 1, the CBP estimator improves the predictive accuracy of three models by about 60%, reducing the standard deviation across all models to below 0.02 fm. This demonstrates the strong global optimization capability of the CBP estimator. To illustrate the progress achieved by the CBP method, Table 1 also presents the optimization performance of the NBP method for comparison. The NBP method is a discrete Bayesian probabilistic approach that employs the *k-means* algorithm to determine cluster centers δ_i , which are then used to refine theoretical models. For the three models, the improvement rate of the CBP method is approximately 10% higher than that of the NBP method. This arises from the CBP estimator treating residuals as continuous variables and obtaining the estimated residual value δ^{em} by integrating the posterior PDF over the entire residual distribution, rather than using a discrete posterior probability as in the NBP method. The CBP estimator accounts for all possible residual contributions, thereby achieving a higher degree of optimization and demonstrating a clear advantage.

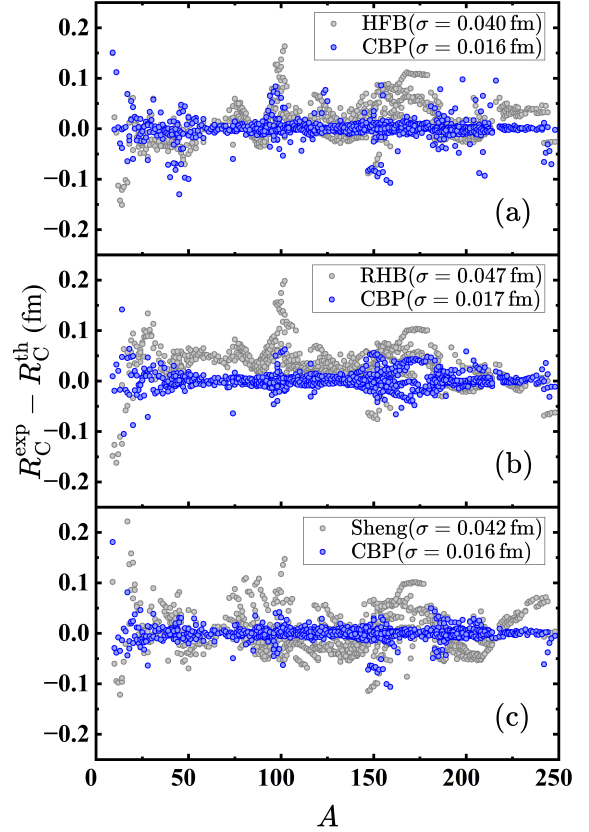


Fig. 1. **a** The charge radii residuals $\delta = R_C^{\text{exp}} - R_C^{\text{th}}$ from the experimental data as a function of mass number A . The grey dots denote the raw results from the HFB calculations, and the blue dots denote the predicted residuals after the CBP refinements. **b** and **c** the same as **a**, but for the results from RHB model and Sheng's formula, respectively.

To further illustrate the performance of the CBP estimator across different models and regions, Fig. 1 presents the raw residuals (gray dots) from the HFB model, the RHB

model and the semi-empirical formula, along with the corrected residuals (blue dots) after applying the CBP estimator. It is evident that, after CBP optimization, the residuals for all three theoretical models are remarkably reduced across most regions. This improvement can be attributed to the CBP estimator's framework. Based on the global description of theoretical models, the CBP estimator utilizes a statistical approach to further capture local correlation effects among nuclei with identical proton or neutron numbers. The introduction of the weight function ensures that only nuclei in close proximity to the target nucleus on the nuclear chart significantly influence the prediction, enhancing the sensitivity of the CBP estimator to local correlation effects. Therefore, the CBP estimator is more effective in regions where local correlations are stronger and the distribution of δ^{pre} is more regular, such as regions with pronounced shell effects.

In regions $60 < A < 90$, $120 < A < 140$, and $215 < A < 240$ in Fig. 1a; $45 < A < 90$, $110 < A < 140$, and $220 < A < 240$ in Fig. 1b; and $80 < A < 95$, $110 < A < 145$, and $210 < A < 240$ in Fig. 1c, where theoretical model predictions exhibit similar accuracy and the distribution of δ^{pre} is highly regular, the CBP estimator achieves substantial improvements, considerably reducing the residuals. In particular, for nuclei with mass numbers around $A = 100$, $A = 150$, and $A = 190$, where proton-neutron residual interactions and other physical effects lead to large δ^{pre} , the CBP method markedly enhances predictive accuracy by statistically accounting for these interactions and effects. However, for light nuclei, where δ^{pre} exhibit greater variability due to relatively low nucleon numbers, the optimization effect of the CBP estimator is comparatively limited. As more charge radii of light nuclei are precisely measured in experiments, the predictive performance of the CBP estimator for light nuclei will be further enhanced.

B. Extrapolating capabilities of the CBP estimator

Model extrapolation is essential for acquiring unknown data. In this section, the extrapolation performance of the CBP estimator is evaluated. The learning set comprises 790 nuclei with proton numbers $Z > 3$ from the 2004 charge radii compilation [10], while the validation set includes 102 experimental charge radii added between 2004 and 2013. The bandwidth parameters h_δ , h_N , and h_Z used in the extrapolation process are the same as those employed in the global optimization. The standard deviations σ_{pre} and σ_{post} for the learning and validation sets, both before and after applying the CBP estimator, are reported in Table 2, along with the optimization rate $\Delta\sigma/\sigma_{\text{pre}}$.

According to Table 2, the standard deviations of R_C calculated by the HFB model, the RHB model, and the semi-empirical formula are approximately 0.040 fm for both the learning and validation sets. This consistency indicates that the initial theoretical models possess considerable extrapolation capabilities. After applying the CBP estimator, the standard deviations for all three models in the learning set decrease to below 0.020 fm, achieving an improvement of ap-

Table 2. The raw standard deviation σ_{pre} (fm) from the theoretical models and the standard deviation σ_{post} (fm) after the CBP estimator refinements. The learning set includes 790 nuclei with $Z > 3$ in the 2004 compilation, and the validation set includes the newly added 102 nuclei in the 2013 compilation.

Models	Learning set			Validation set		
	σ_{pre}	σ_{post}	$\Delta\sigma/\sigma_{\text{pre}}$	σ_{pre}	σ_{post}	$\Delta\sigma/\sigma_{\text{pre}}$
HFB	0.040	0.017	57.5%	0.038	0.021	44.7%
RHB	0.046	0.017	63.0%	0.052	0.025	51.9%
Sheng	0.042	0.018	57.1%	0.043	0.026	39.5%

proximately 60% compared to the initial results. In the validation set, the standard deviations are slightly above 0.020 fm, with improvement rates around 45% for the three models. The steady improvement rates across both the learning and validation sets demonstrate the robust extrapolative capabilities of the CBP estimator.

The optimization rates for all three models in the validation set are lower than those in the learning set. This phenomenon can be explained by the CBP framework: the Bayesian formula accounts for statistical correlations among nuclei with the same proton and neutron numbers, while the weight function considers local relationships among neighboring nuclei. Most nuclei in the validation set are positioned near the drip line, where fewer neighboring nuclei are represented in the learning set, thereby diminishing the performance of the CBP estimator. As more R_C values are measured in experiments, the extrapolation ability of the CBP estimator is expected to improve significantly.

The results in Table 2 indicate that the CBP estimator demonstrates excellent extrapolation capabilities. The HFB model, the RHB model and the semi-empirical formula provide the overall trend of R_C variations. By inheriting the advantages of theoretical models and incorporating local correlation characteristics between nuclei, the CBP estimator captures physical effects not reflected in theoretical models, leading to reliable corrections of R_C . As a result, for nuclei lacking experimental data, the CBP estimator can offer precise and robust predictions.

C. Comprehensively factoring in the results of different models using the BMA method

After optimization using the CBP estimator, specific models exhibit optimal predictive performance in distinct regions, especially for nuclei far from the β -stability line. This study introduces the BMA method to integrate these strengths. The BMA method assigns weights based on the predictive performance of different models for benchmark nuclei, thereby balancing the predictive discrepancies among theoretical models across different regions of the nuclear chart. The benchmark nuclei selected for the BMA method are ^{49}K , ^{38}Ca , ^{119}Cd , and ^{201}Po , covering a wide range of the nuclear chart, spanning from light to heavy nuclei and from proton-rich to neutron-rich regions. These nuclei are located near the edges

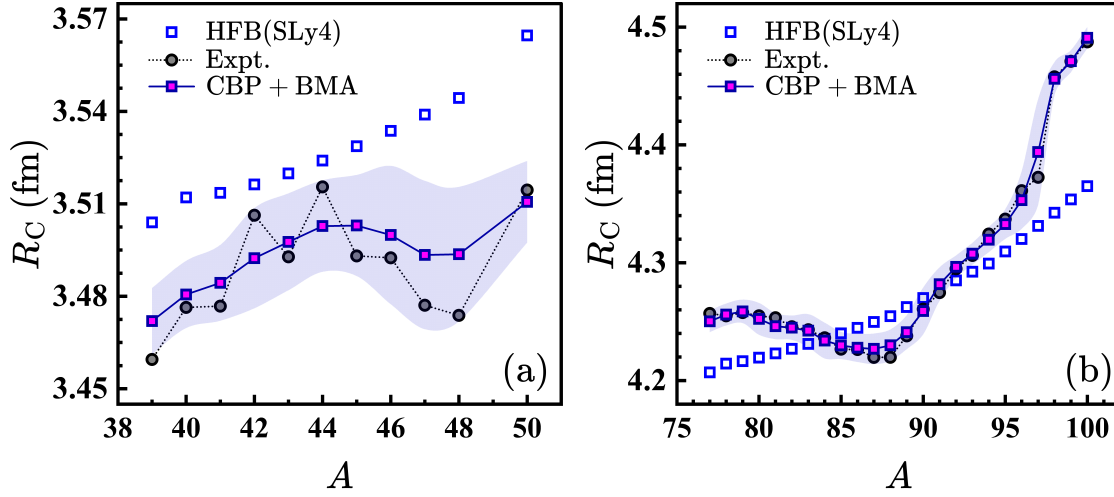


Fig. 2. **a** The theoretical and experimental charge radii R_C for Ca isotopes, with uncertainty bands included for the predictions refined by the CBP estimator. **b** Similar to **a**, but for Sr isotopes.

of the nuclear chart and are outside the 2013 charge radii compilation, making them particularly valuable for benchmarking extrapolation capabilities.

After obtaining the corrected residuals $\delta^{\text{corr}} = R_C^{\text{exp}} - R_C^{\text{corr}}$ for the benchmark nuclei, the weights for each model are calculated using the BMA method, with the results presented in Table 3. The HFB model exhibits superior predictive accuracy for the benchmark nuclei and is thus assigned higher weights. In contrast, the RHB model and the semi-empirical formula are assigned lower weights due to their lower predictive accuracy. The BMA method was applied to optimize predictions for 102 validation nuclei. The standard deviation is 0.020 fm, which is lower than that from the individual model optimized by the CBP estimator, as shown in Table 2. Compared with the HFB model, the RHB model, and Sheng's formula individually optimized using the CBP estimator, the introduction of the BMA method improves the accuracy by 5%, 20%, and 23%, respectively. This demonstrates that the BMA method effectively combines the strengths of different models, further enhancing predictive accuracy.

Table 3. The corrected residuals δ^{corr} (fm) of four benchmark nuclei: ^{49}K , ^{38}Ca , ^{119}Cd , and ^{201}Po , and the weights of three models by BMA are based on δ^{corr} of these four benchmark nuclei.

Models	^{49}K	^{38}Ca	^{119}Cd	^{201}Po	Weight
HFB	0.017	-0.003	0.007	0.007	0.58
RHB	-0.015	0.010	-0.006	-0.017	0.25
Sheng	0.013	0.013	0.010	0.018	0.17

Analyzing the trend of variation in charge radii within isotopic chains reveals many important and interesting physical phenomena. This study combines the CBP and BMA methods to predict the R_C of the Ca and Sr isotopic chains, illustrating the capability of this approach to capture the physical effects within isotopic chains. The calcium isotopic chain

serves as a distinctive nuclear system for investigating the interactions between protons and neutrons inside the nucleus [81–83]. In the stable isotope region of the Ca chain, ^{40}Ca and ^{48}Ca both exhibit magic numbers of protons and neutrons, and their R_C are nearly identical. Due to the change in nuclear structure associated with the shell closure, a kink in R_C at $N = 28$ is observed. For $20 < N < 28$, the trend of R_C follows a parabolic-like shape, and the odd-even staggering effect on R_C is particularly pronounced. For neutron-rich nuclei with $N > 28$, R_C exhibits a strong increase.

Fig. 2a presents the predicted charge radii \bar{R} (purple squares) for the Ca isotopic chain based on the combined CBP and BMA methods, along with uncertainty bands calculated from the corresponding error estimates. The experimental values R_C^{exp} (gray circles) and the initial results from the HFB model (blue squares) are also provided for comparison. The HFB model predicts an approximately linear relationship between R_C and the mass number, which evidently deviates from experimental results. After corrections using the CBP and BMA methods, the discrepancies between \bar{R} and experimental data are substantially reduced, providing an accurate description of the parabolic trend of R_C and the kink at ^{48}Ca .

Apart from the Ca isotopes, the charge radii of Sr isotopes also exhibit prominent shell effects [84]. The Sr isotope chain extends from the valley of stability at ^{88}Sr , where isotopes show a spherical shape, to strongly deformed isotopes on either side of the stability line. As the nucleus approaches the neutron shell closure at $N = 50$ from the neutron-deficient side, R_C gradually decreases. At $N = 50$, it exhibits a kink, after which it begins to increase. When N reaches 60, a sudden increase in R_C is observed, corresponding to an experimental transition from a near-spherical shape to a strongly deformed configuration. The refined predictions \bar{R} of Sr isotopes obtained using the CBP estimator in conjunction with the BMA approach are shown in Fig. 2b. The \bar{R} are closely align with experimental data, particularly for the kink of ^{88}Sr and the pronounced increase in R_C observed at ^{98}Sr .

IV. SUMMARY

This study combines the continuous Bayesian probability (CBP) estimator with the Bayesian model averaging (BMA) to refine R_C predictions from the HFB model, the RHB model, and the semi-empirical formula. In global optimization, the CBP estimator achieves approximately 60% improvement for all three models. In extrapolation, it demonstrates improvement rates of around 45%. These results indicate that, grounded in sophisticated theoretical models, the CBP estimator can provide accurate predictions of R_C in unknown regions of the nuclear chart. To enhance predictive accuracy for nuclei near the drip line, the BMA method is subsequently employed to assign weights to each model based on their predictive performance for benchmark nuclei. By combining the CBP estimator with the BMA method, the standard deviation is further reduced, and physical phenomena on R_C such as shell effects in the Ca and Sr isotopic chains are accurately captured.

The improvements achieved by the proposed method are

attributed to the theoretical frameworks of the CBP estimator and the BMA method. According to the CBP estimator framework, a continuous posterior probability density function (PDF) is generated to obtain the estimated residuals for the target nucleus. The Bayesian formula captures the statistical relationships among nuclei with the same proton or neutron number, while the weight function accounts for local correlations among neighboring nuclei. Theoretical models provide the overall trend of R_C , and the CBP estimator reliably refines these theoretical results through statistical techniques. On this basis, the BMA method combines the strengths of different models across various regions of the nuclear chart, leading to further refinement of the results.

In summary, the CBP and BMA methods have been effectively employed to predict nuclear masses and charge radii, demonstrating considerable predictive accuracy. The methodologies developed in this work can be further extended to estimate charge radii in regions far from the β -stability line and are equally applicable to the exploration of other nuclear properties, including nuclear reactions and decay processes.

-
- [1] M. Bender, P. H. Heenen, P. G. Reinhard, Self-consistent mean-field models for nuclear structure. *Rev. Mod. Phys.* **75**, 121–180 (2003). doi: [10.1103/RevModPhys.75.121](https://doi.org/10.1103/RevModPhys.75.121)
 - [2] K. Heyde, J. L. Wood, Shape coexistence in atomic nuclei. *Rev. Mod. Phys.* **83**, 1467–1521 (2011). doi: [10.1103/RevModPhys.83.1467](https://doi.org/10.1103/RevModPhys.83.1467)
 - [3] S. J. Novario, D. Lonardonì, S. Gandolfi, et al., Trends of Neutron Skins and Radii of Mirror Nuclei from First Principles. *Phys. Rev. Lett.* **130**, 032501 (2023). doi: [10.1103/PhysRevLett.130.032501](https://doi.org/10.1103/PhysRevLett.130.032501)
 - [4] M. Q. Ding, D. Q. Fang, Y. G. Ma, Neutron skin and its effects in heavy-ion collisions. *Nucl. Sci. Tech.* **35**, 211 (2024). doi: [10.1007/s41365-024-01584-1](https://doi.org/10.1007/s41365-024-01584-1)
 - [5] W. Geithner, T. Neff, G. Audi, et al., Masses and Charge Radii of $^{17-22}\text{Ne}$ and the Two-Proton-Halo Candidate ^{17}Ne . *Phys. Rev. Lett.* **101**, 252502 (2008). doi: [10.1103/PhysRevLett.101.252502](https://doi.org/10.1103/PhysRevLett.101.252502)
 - [6] T. Otsuka, A. Gade, O. Sorlin, et al., Evolution of shell structure in exotic nuclei. *Rev. Mod. Phys.* **92**, 015002 (2020). doi: [10.1103/RevModPhys.92.015002](https://doi.org/10.1103/RevModPhys.92.015002)
 - [7] R. P. de Groote, J. Billowes, C. L. Binnersley, et al., Measurement and microscopic description of odd-even staggering of charge radii of exotic copper isotopes. *Nat. Phys.* **16**, 620–624 (2020). doi: [10.1038/s41567-020-0868-y](https://doi.org/10.1038/s41567-020-0868-y)
 - [8] R. An, X. Jiang, L. G. Cao, F. S. Zhang, Odd-even staggering and shell effects of charge radii for nuclei with even Z from 36 to 38 and from 52 to 62. *Phys. Rev. C* **105**, 014325 (2022). doi: [10.1103/PhysRevC.105.014325](https://doi.org/10.1103/PhysRevC.105.014325)
 - [9] A. Ekström, G. Hagen, T. D. Morris, et al., Δ isobars and nuclear saturation. *Phys. Rev. C* **97**, 024332 (2018). doi: [10.1103/PhysRevC.97.024332](https://doi.org/10.1103/PhysRevC.97.024332)
 - [10] I. Angeli, A consistent set of nuclear rms charge radii: properties of the radius surface $R(N,Z)$. *At. Data Nucl. Data Tables* **87**, 185–206 (2004). doi: [10.1016/j.adt.2004.04.002](https://doi.org/10.1016/j.adt.2004.04.002)
 - [11] I. Sick, Elastic electron scattering from light nuclei. *Prog. Part. Nucl. Phys.* **47**, 245–318 (2001). doi: [10.1016/S0146-6410\(01\)00156-9](https://doi.org/10.1016/S0146-6410(01)00156-9)
 - [12] K. Tsukada, Y. Abe, A. Enokizono, et al., First Observation of Electron Scattering from Online-Produced Radioactive Target. *Phys. Rev. Lett.* **131**, 092502 (2023). doi: [10.1103/PhysRevLett.131.092502](https://doi.org/10.1103/PhysRevLett.131.092502)
 - [13] G. Fricke, C. Bernhardt, K. Heilig, et al., Nuclear Ground State Charge Radii from Electromagnetic Interactions. *At. Data Nucl. Data Tables* **60**, 177–285 (1995). doi: [10.1006/adnd.1995.1007](https://doi.org/10.1006/adnd.1995.1007)
 - [14] A. Krieger, K. Blaum, M. L. Bissell, et al., Nuclear Charge Radius of ^{12}Be . *Phys. Rev. Lett.* **108**, 142501 (2012). doi: [10.1103/PhysRevLett.108.142501](https://doi.org/10.1103/PhysRevLett.108.142501)
 - [15] I. Angeli, K. P. Marinova, Table of experimental nuclear ground state charge radii: An update. *At. Data Nucl. Data Tables* **99**, 69–95 (2013). doi: [10.1016/j.adt.2011.12.006](https://doi.org/10.1016/j.adt.2011.12.006)
 - [16] T. Li, Y. Luo, N. Wang, Compilation of recent nuclear ground state charge radius measurements and tests for models. *At. Data Nucl. Data Tables* **140**, 101440 (2021). doi: [10.1016/j.adt.2021.101440](https://doi.org/10.1016/j.adt.2021.101440)
 - [17] K. König, J. C. Berengut, A. Borschevsky, et al., Nuclear Charge Radii of Silicon Isotopes. *Phys. Rev. Lett.* **132**, 162502 (2024). doi: [10.1103/PhysRevLett.132.162502](https://doi.org/10.1103/PhysRevLett.132.162502)
 - [18] P. Plattner, E. Wood, L. Al Ayoubi, et al., Nuclear Charge Radius of ^{26m}Al and Its Implication for V_{ud} in the Quark Mixing Matrix. *Phys. Rev. Lett.* **131**, 222502 (2023). doi: [10.1103/PhysRevLett.131.222502](https://doi.org/10.1103/PhysRevLett.131.222502)
 - [19] K. König, S. Fritzsche, G. Hagen, et al., Surprising Charge-Radius Kink in the Sc Isotopes at $N = 20$. *Phys. Rev. Lett.* **131**, 102501 (2023). doi: [10.1103/PhysRevLett.131.102501](https://doi.org/10.1103/PhysRevLett.131.102501)
 - [20] J. G. Cubiss, A. N. Andreyev, A. E. Barzakh, et al., Deformation versus Sphericity in the Ground States of the Lightest Gold Isotopes. *Phys. Rev. Lett.* **131**, 202501 (2023). doi: [10.1103/PhysRevLett.131.202501](https://doi.org/10.1103/PhysRevLett.131.202501)
 - [21] N. Wang, T. Li, Shell and isospin effects in nuclear charge radii. *Phys. Rev. C* **88**, 011301 (2013). doi: [10.1103/PhysRevC.88.011301](https://doi.org/10.1103/PhysRevC.88.011301)
 - [22] Z. Q. Sheng, G. G. Fan, J. F. Qian, et al., An effective formula for nuclear charge radii. *Eur. Phys. J. A* **51**, 40 (2015). doi: [10.1140/epja/i2015-12001-1](https://doi.org/10.1140/epja/i2015-12001-1)

- 10.1140/epja/i2015-15040-1
- [23] B. H. Sun, Y. Lu, J. P. Peng, et al., New charge radius relations for atomic nuclei. *Phys. Rev. C* **90**, 054318 (2014). doi: 10.1103/PhysRevC.90.054318
- [24] M. Bao, Y. Lu, Y. M. Zhao, A. Arima, Predictions of nuclear charge radii. *Phys. Rev. C* **94**, 064315 (2016). doi: 10.1103/PhysRevC.94.064315
- [25] M. Bao, Y. Y. Zong, Y. M. Zhao, et al., Local relations of nuclear charge radii. *Phys. Rev. C* **102**, 014306 (2020). doi: 10.1103/PhysRevC.102.014306
- [26] C. Ma, Y. Y. Zong, Y. M. Zhao, et al., Evaluation of nuclear charge radii based on nuclear radii changes. *Phys. Rev. C* **104**, 014303 (2021). doi: 10.1103/PhysRevC.104.014303
- [27] J. Barea, A. Frank, J. G. Hirsch, et al., Garvey-Kelson relations and the new nuclear mass tables. *Phys. Rev. C* **77**, 041304 (2008). doi: 10.1103/PhysRevC.77.041304
- [28] J. Piekarewicz, M. Centelles, X. Roca-Maza, et al., Garvey-Kelson relations for nuclear charge radii. *Eur. Phys. J. A* **46**, 379–386 (2010). doi: 10.1140/epja/i2010-11051-8
- [29] C. Xu, M. Bao, Improved mass relations of mirror nuclei. *Nucl. Sci. Tech.* **35**, 157 (2024). doi: 10.1007/s41365-024-01501-6
- [30] P. Bano, S. P. Pattnaik, M. Centelles, et al., Correlations between charge radii differences of mirror nuclei and stellar observables. *Phys. Rev. C* **108**, 015802 (2023). doi: 10.1103/PhysRevC.108.015802
- [31] M. V. Stoitsov, J. Dobaczewski, W. Nazarewicz, et al., Systematic study of deformed nuclei at the drip lines and beyond. *Phys. Rev. C* **68**, 054312 (2003). doi: 10.1103/PhysRevC.68.054312
- [32] S. Goriely, N. Chamel, J. M. Pearson, Further explorations of Skyrme-Hartree-Fock-Bogoliubov mass formulas. XVI. Inclusion of self-energy effects in pairing. *Phys. Rev. C* **93**, 034337 (2016). doi: 10.1103/PhysRevC.93.034337
- [33] R. Shou, X. Yin, C. Ma, M. Q. Lin, Y. M. Zhao, Simple corrections in theoretical models of atomic masses and nuclear charge radii. *Phys. Rev. C* **106**, L061304 (2022). doi: 10.1103/PhysRevC.106.L061304
- [34] L. S. Geng, H. Toki, S. Sugimoto, et al., Relativistic Mean Field Theory for Deformed Nuclei with Pairing Correlations. *Prog. Theor. Phys* **110**, 921–936 (2003). doi: 10.1143/PTP.110.921
- [35] X. Z. Wang, Q. L. Niu, J. J. Zhang, et al., Nucleon momentum distribution of ^{56}Fe from the axially deformed relativistic mean-field model with nucleon-nucleon correlations. *Sci. China Phys. Mech. Astron.* **64**, 292011 (2021). doi: 10.1007/s11433-021-1729-5
- [36] Y. T. Rong, Accuracy of the mean-field theory in describing ground-state properties of light nuclei. *Phys. Rev. C* **108**, 054314 (2023). doi: 10.1103/PhysRevC.108.054314
- [37] X. W. Xia, Y. Lim, P. W. Zhao, et al., The limits of the nuclear landscape explored by the relativistic continuum Hartree-Bogoliubov theory. *At. Data Nucl. Data Tables* **121-122**, 1–215 (2018). doi: 10.1016/j.adt.2017.09.001
- [38] P. Jiang, Z. M. Niu, Y. F. Niu, W. H. Long, Strutinsky shell correction energies in relativistic Hartree-Fock theory. *Phys. Rev. C* **98**, 064323 (2018). doi: 10.1103/PhysRevC.98.064323
- [39] X. Y. Zhang, Z. M. Niu, W. Sun, et al., Nuclear charge radii and shape evolution of Kr and Sr isotopes with the deformed relativistic Hartree-Bogoliubov theory in continuum. *Phys. Rev. C* **108**, 024310 (2023). doi: 10.1103/PhysRevC.108.024310
- [40] B. N. Lu, N. Li, S. Elhatisari, et al., Ab Initio Nuclear Thermodynamics. *Phys. Rev. Lett.* **125**, 192502 (2020). doi: 10.1103/PhysRevLett.125.192502
- [41] B. R. Barrett, P. Navrátil, J. P. Vary, Ab initio no core shell model. *Prog. Part. Nucl. Phys.* **69**, 131–181 (2013). doi: 10.1016/j.ppnp.2012.10.003
- [42] A. Boehnlein, M. Diefenthaler, N. Sato, et al., Colloquium: Machine learning in nuclear physics. *Rev. Mod. Phys.* **94**, 031003 (2022). doi: 10.1103/RevModPhys.94.031003
- [43] W. B. He, Q. F. Li, Y. G. Ma, et al., Machine learning in nuclear physics at low and intermediate energies. *Sci. China Phys. Mech. Astron.* **66**, 282001 (2023). doi: 10.1007/s11433-023-2116-0
- [44] L. Neufcourt, Y. C. Cao, W. Nazarewicz, et al., Bayesian approach to model-based extrapolation of nuclear observables. *Phys. Rev. C* **98**, 034318 (2018). doi: 10.1103/PhysRevC.98.034318
- [45] L. Neufcourt, Y. C. Cao, S. Giuliani, et al., Beyond the proton drip line: Bayesian analysis of proton-emitting nuclei. *Phys. Rev. C* **101**, 014319 (2020). doi: 10.1103/PhysRevC.101.014319
- [46] Z. M. Niu, J. Y. Fang, Y. F. Niu, Comparative study of radial basis function and Bayesian neural network approaches in nuclear mass predictions. *Phys. Rev. C* **100**, 054311 (2019). doi: 10.1103/PhysRevC.100.054311
- [47] X. H. Wu, P. W. Zhao, Predicting nuclear masses with the kernel ridge regression. *Phys. Rev. C* **101**, 051301 (2020). doi: 10.1103/PhysRevC.101.051301
- [48] Y. H. Lu, T. S. Shang, P. X. Du, et al., Nuclear mass predictions based on convolutional neural network. *arXiv:2404.14948 [nucl-th]* (2024). <https://arxiv.org/abs/2404.14948>
- [49] X. C. Ming, H. F. Zhang, R. R. Xu, et al., Nuclear mass based on the multi-task learning neural network method. *Nucl. Sci. Tech.* **33**, 48 (2022). doi: 10.1007/s41365-022-01031-z
- [50] Z. P. Gao, Y. J. Wang, H. L. Lü, et al., Machine learning the nuclear mass. *Nucl. Sci. Tech.* **32**, 109 (2021). doi: 10.1007/s41365-021-00956-1
- [51] E. Yüksel, D. Soydaner, H. Bahtiyar, et al., Nuclear mass predictions using machine learning models. *Phys. Rev. C* **109**, 064322 (2024). doi: 10.1103/PhysRevC.109.064322
- [52] T. S. Shang, J. Li, Z. M. Niu, Prediction of nuclear charge density distribution with feedback neural network. *Nucl. Sci. Tech.* **33**, 153 (2022). doi: 10.1007/s41365-022-01140-9
- [53] T. S. Shang, H. H. Xie, J. Li, et al., Global prediction of nuclear charge density distributions using a deep neural network. *Phys. Rev. C* **110**, 014308 (2024). doi: 10.1103/PhysRevC.110.014308
- [54] Z. S. Jin, M. S. Yan, H. Zhou, et al., Bayesian optimization approach to model-based description of α decay. *Phys. Rev. C* **108**, 014326 (2023). doi: 10.1103/PhysRevC.108.014326
- [55] Z. M. Niu, H. Z. Liang, B. H. Sun, et al., Predictions of nuclear β -decay half-lives with machine learning and their impact on r -process nucleosynthesis. *Phys. Rev. C* **99**, 064307 (2019). doi: 10.1103/PhysRevC.99.064307
- [56] B. S. Cai, C. X. Yuan, Random forest-based prediction of decay modes and half-lives of superheavy nuclei. *Nucl. Sci. Tech.* **34**, 204 (2023). doi: 10.1007/s41365-023-01354-5
- [57] J. M. Munoz, S. Akkoyun, Z. P. Reyes, et al., Predicting β -decay energy with machine learning. *Phys. Rev. C* **107**, 034308 (2023). doi: 10.1103/PhysRevC.107.034308
- [58] Z. A. Wang, J. C. Pei, Optimizing multilayer Bayesian neural networks for evaluation of fission yields. *Phys. Rev. C* **104**, 064608 (2021). doi: 10.1103/PhysRevC.104.064608
- [59] Z. A. Wang, J. C. Pei, Y. J. Chen, et al., Bayesian approach to heterogeneous data fusion of imperfect fission yields for augmented evaluations. *Phys. Rev. C* **106**, L021304 (2022). doi: 10.1103/PhysRevC.106.L021304

- [60] C. Y. Qiao, J. C. Pei, Z. A. Wang, et al., Bayesian evaluation of charge yields of fission fragments of ^{239}U . *Phys. Rev. C* **103**, 034621 (2021). doi: [10.1103/PhysRevC.103.034621](https://doi.org/10.1103/PhysRevC.103.034621)
- [61] S. Akkoyun, T. Bayram, S. O. Kara, et al., An artificial neural network application on nuclear charge radii. *J. Phys. G Nucl. Part. Phys.* **40**, 055106 (2013). doi: [10.1088/0954-3899/40/5/055106](https://doi.org/10.1088/0954-3899/40/5/055106)
- [62] R. Utama, W. C. Chen, J. Piekarewicz, Nuclear charge radii: density functional theory meets Bayesian neural networks. *J. Phys. G Nucl. Part. Phys.* **43**, 114002 (2016). doi: [10.1088/0954-3899/43/11/114002](https://doi.org/10.1088/0954-3899/43/11/114002)
- [63] X. X. Dong, R. An, J. X. Lu, et al., Novel Bayesian neural network based approach for nuclear charge radii. *Phys. Rev. C* **105**, 014308 (2022). doi: [10.1103/PhysRevC.105.014308](https://doi.org/10.1103/PhysRevC.105.014308)
- [64] X. X. Dong, R. An, J. X. Lu, et al., Nuclear charge radii in Bayesian neural networks revisited. *Phys. Lett. B* **838**, 137726 (2023). doi: [10.1016/j.physletb.2023.137726](https://doi.org/10.1016/j.physletb.2023.137726)
- [65] Y. Y. Cao, J. Y. Guo, B. Zhou, Predictions of nuclear charge radii based on the convolutional neural network. *Nuc. Sci. Tech.* **34**, 152 (2023). doi: [10.1007/s41365-023-01308-x](https://doi.org/10.1007/s41365-023-01308-x)
- [66] X. Zhang, H. He, G. Qu, et al., Investigation of the difference in charge radii of mirror pairs with deep Bayesian neural networks. *Phys. Rev. C* **110**, 014316 (2024). doi: [10.1103/PhysRevC.110.014316](https://doi.org/10.1103/PhysRevC.110.014316)
- [67] L. Tang, Z. H. Zhang, Nuclear charge radius predictions by kernel ridge regression with odd–even effects. *Nucl. Sci. Tech.* **35**, 19 (2024). doi: [10.1007/s41365-024-01379-4](https://doi.org/10.1007/s41365-024-01379-4)
- [68] Y. F. Ma, C. Su, J. Liu, et al., Predictions of nuclear charge radii and physical interpretations based on the naive Bayesian probability classifier. *Phys. Rev. C* **101**, 014304 (2020). doi: [10.1103/PhysRevC.101.014304](https://doi.org/10.1103/PhysRevC.101.014304)
- [69] Y. F. Liu, C. Su, J. Liu, et al., Improved naive Bayesian probability classifier in predictions of nuclear mass. *Phys. Rev. C* **104**, 014315 (2021). doi: [10.1103/PhysRevC.104.014315](https://doi.org/10.1103/PhysRevC.104.014315)
- [70] J. Z. Xie, K. P. Wang, C. Wang, et al., Novel Bayesian probability method in predictions of nuclear masses. *Phys. Rev. C* **109**, 064317 (2024). doi: [10.1103/PhysRevC.109.064317](https://doi.org/10.1103/PhysRevC.109.064317)
- [71] Y. Saito, I. Dillmann, R. Krücken, et al., Uncertainty quantification of mass models using ensemble Bayesian model averaging. *Phys. Rev. C* **109**, 054301 (2024). doi: [10.1103/PhysRevC.109.054301](https://doi.org/10.1103/PhysRevC.109.054301)
- [72] L. Neufcourt, Y. Cao, W. Nazarewicz, et al., Neutron Drip Line in the Ca Region from Bayesian Model Averaging. *Phys. Rev. Lett.* **122**, 062502 (2019). doi: [10.1103/PhysRevLett.122.062502](https://doi.org/10.1103/PhysRevLett.122.062502)
- [73] E. Alhassan, D. Rochman, G. Schnabel, et al., Bayesian model averaging (BMA) for nuclear data evaluation. *Nucl. Sci. Tech.* **35**, 205 (2024). doi: [10.1007/s41365-024-01543-w](https://doi.org/10.1007/s41365-024-01543-w)
- [74] D. M. Rossi, K. Minamisono, H. B. Asberry, et al., Charge radii of neutron-deficient ^{36}K and ^{37}K . *Phys. Rev. C* **92**, 014305 (2015). doi: [10.1103/PhysRevC.92.014305](https://doi.org/10.1103/PhysRevC.92.014305)
- [75] A. J. Miller, K. Minamisono, A. Klose, et al., Proton superfluidity and charge radii in proton-rich calcium isotopes. *Nat. Phys.* **15**, 432–436 (2019). doi: [10.1038/s41567-019-0416-9](https://doi.org/10.1038/s41567-019-0416-9)
- [76] M. Hammen, W. Nörtershäuser, D. L. Balabanski, et al., From Calcium to Cadmium: Testing the Pairing Functional through Charge Radii Measurements of $^{100-130}\text{Cd}$. *Phys. Rev. Lett.* **121**, 102501 (2018). doi: [10.1103/PhysRevLett.121.102501](https://doi.org/10.1103/PhysRevLett.121.102501)
- [77] M. D. Seliverstov, T. E. Cocolios, W. Dexters, et al., Charge radii of odd-A Po isotopes. *Phys. Lett. B* **719**, 362–366 (2013). doi: [10.1016/j.physletb.2013.01.043](https://doi.org/10.1016/j.physletb.2013.01.043)
- [78] P. W. Zhao, Z. P. Li, J. M. Yao, et al., New parametrization for the nuclear covariant energy density functional with a point-coupling interaction. *Phys. Rev. C* **82**, 054319 (2010). doi: [10.1103/PhysRevC.82.054319](https://doi.org/10.1103/PhysRevC.82.054319)
- [79] H. H. Xie, J. Li, L. G. Jiao, et al., Finite-nuclear-size effect in hydrogenlike ions with relativistic nuclear structure. *Phys. Rev. A* **107**, 042807 (2023). doi: [10.1103/PhysRevA.107.042807](https://doi.org/10.1103/PhysRevA.107.042807)
- [80] H. H. Xie, J. Li, Impact of intrinsic electromagnetic structure on the nuclear charge radius in relativistic density functional theory. *Phys. Rev. C* **110**, 064319 (2024). doi: [10.1103/PhysRevC.110.064319](https://doi.org/10.1103/PhysRevC.110.064319)
- [81] R. F. Garcia Ruiz, M. L. Bissell, K. Blaum, et al., Unexpectedly large charge radii of neutron-rich calcium isotopes. *Nat. Phys.* **12**, 594–598 (2016). doi: [10.1038/nphys3645](https://doi.org/10.1038/nphys3645)
- [82] G. Co', M. Anguiano, A. M. Lallena, Charge radii of Ca isotopes and correlations. *Phys. Rev. C* **105**, 034320 (2022). doi: [10.1103/PhysRevC.105.034320](https://doi.org/10.1103/PhysRevC.105.034320)
- [83] T. Inakura, N. Hinohara, H. Nakada, Radial and orbital decomposition of charge radii of Ca nuclei: Comparative study of Skyrme and Fayans functionals. *Phys. Rev. C* **110**, 054315 (2024). doi: [10.1103/PhysRevC.110.054315](https://doi.org/10.1103/PhysRevC.110.054315)
- [84] R. E. Silverans, P. Lievens, L. Vermeeren, et al., Nuclear Charge Radii of $^{78-100}\text{Sr}$ by Nonoptical Detection in Fast-Beam Laser Spectroscopy. *Phys. Rev. Lett.* **60**, 2607–2610 (1988). doi: [10.1103/PhysRevLett.60.2607](https://doi.org/10.1103/PhysRevLett.60.2607)